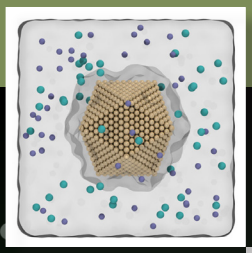

Nucleation, growth, and superlattice formation of nanocrystals observed in liquid cell transmission electron microscopy

Qian Chen, Jong Min Yuk, Matthew R. Hauwiller, Jungjae Park, Kyun Seong Dae, Jae Sung Kim, and A. Paul Alivisatos

This article reviews the advancements and prospects of liquid cell transmission electron microscopy (TEM) imaging and analysis methods in understanding the nucleation, growth, etching, and assembly dynamics of nanocrystals. The bonding of atoms into nanoscale crystallites produces materials with nonadditive properties unique to their size and geometry. The recent application of *in situ* liquid cell TEM to nanocrystal development has initiated a paradigm shift, (1) from trial-and-error synthesis to a mechanistic understanding of the "synthetic reactions" responsible for the emergence of crystallites from a disordered soup of reactive species (e.g., ions, atoms, molecules) and shape-defined growth or etching; and (2) from post-processing characterization of the nanocrystals' superlattice assemblies to *in situ* imaging and mapping of the fundamental interactions and energy landscape governing their collective phase behaviors. Imaging nanocrystal formation and assembly processes on the single-particle level in solution immediately impacts many existing fields, including materials science, nanochemistry, colloidal science, biology, environmental science, electrochemistry, mineralization, soft condensed-matter physics, and device fabrication.

Introduction

Archaeologists study fossils to recreate history of ecologies, evolutionary events, and climate. Underneath the static structure, the shapes and compositions of fossils are temporal series of forming and deforming governed by environmental factors. On a shorter time scale, materials scientists make nanocrystals out of self-organization of atoms to harness their size and shape-specific optical, electronic and magnetic properties,[1–7] or further use the nanocrystals as "artificial atoms" to build higher-order crystalline forms of superlattices,[8–10] where the properties of each component nanocrystal couple and hybridize collectively. These nanomaterials also have their structure, shape, and composition encoded by a temporal series of kinetic events during their synthesis, such as nucleation, coalescence, and interconversion among metastable structures.

These events occur at the atomic or nanoscale in a suspended solvent medium, involving dynamic diffusion and interaction of atoms, clusters, or nanocrystals. Resolving and understanding these events will enable predictable control over low-cost and facile bottom-up methods to synthesize functional nanomaterials useful for drug delivery, bioimaging, electronics, photonics, and sensors.[11–18] Moreover, knowledge on how the kinetic pathways govern the materials synthesis can potentially enable the theme of "free energy landscape engineering," where not only the final equilibrium structure, but also the series of metastable states, the depth of local traps, and the interconversion kinetics are better understood. This theme carries the immediate promise of making synthesis more precise, more efficient, and of higher yield. More importantly, one can identify the key kinetic and energetic parameters to

Qian Chen, Department of Materials Science and Engineering, University of Illinois at Urbana-Champaign, USA; qchen20@illinois.edu
Jong Min Yuk, Department of Materials Science and Engineering, Korea Advanced Institute of Science and Technology, Korea; jongmin.yuk@kaist.ac.kr
Matthew R. Hauwiller, Department of Materials Science and Engineering, Massachusetts Institute of Technology, USA; mhauwill@mit.edu
Jungjae Park, Department of Materials Science and Engineering, Korea Advanced Institute of Science and Technology, Korea; jungjae10@kaist.ac.kr
Kyun Seong Dae, Department of Materials Science and Engineering, Korea Advanced Institute of Science and Technology, Korea; ddalgi1051@kaist.ac.kr
Jae Sung Kim, Department of Materials Science and Engineering, Korea Advanced Institute of Science and Technology, Korea; ijs7596@kaist.ac.kr
A. Paul Alivisatos, University of California, Berkeley; Kavli Energy Nanoscience Institute; Lawrence Berkeley National Laboratory, USA; paul.alivisatos@berkeley.edu
doi:10.1557/mrs.2020.229

realize improved materials via inverse design.[19,20] An example of such a material that thus far has limited experimental realization are the highly sought-after open superlattices consisting of periodic holes, due to their light weight, high porosity, low thermal conductivity, and highly tailorable stress–strain response and photonic bandgap for applications in catalysis, photonics, and metamaterials.[21–23]

For decades, the strategy used to understand the formation mechanism of these nanomaterials has been limited to what archaeologists do—analyzing and tracing hints in the final products. A set of empirical rules has been accumulated and established for nanocrystal growth thanks to the enormous synthetic efforts of chemists. If nanocrystals are nonspherical in shape (e.g., cubes, plates, and rods) despite symmetric atom packing (e.g., face-centered cubic for most noble metals), facet-dependent growth rates has often been inferred as the controlling factor during the synthesis.[1,24] This anisotropy in growth rates is attributed qualitatively to selective coordination of molecular species onto certain facets of the growing nanocrystals. Likewise, for growth of multicomponent nanocrystals (e.g., rods, dumbbells, tetrapods)[25–29] as selective catalysts[30,31] or self-propelled nanomachines,[32] synthesis is often ascribed to high lattice mismatch that induces partial deposition of one component over the other, similar to the monolayer to island growth transition in the Stranski–Krastanov model of thin-film epitaxy.[33]

These empirical rules, although helpful to rationalize certain trends, lack quantitative understanding and validation, making synthetic efforts largely heuristic. Modeling and simulation of nanocrystal growth are difficult because one needs to consider the collective effects of factors on multiple length scales, from molecular reactions, to mass transport, solvation, intermolecular interaction, to surface and interface energies. Ensemble spectroscopy methods measure kinetic reaction rates to determine rate-limiting steps and to compare with classical nucleation theory (CNT). These methods do not consider other properties such as morphology control and surface structures of nanocrystals, let alone the nearly universal heterogeneity at the single nanocrystal level. Similar challenges exist for superlattice formation out of nanocrystals. Ensemble scattering techniques such as small-angle x-ray scattering (SAXS)[34,35] and grazing-incidence x-ray scattering[36–38] can monitor the averaged ensemble structural evolution of the superlattice in solvent conditions in reciprocal space, but does not resolve the spatially heterogeneous local density and ordering fluctuation that eventually leads to initial nucleation and crystallite growth.

The recent emergence of liquid phase atomic force microscopy (AFM) has shown great power in imaging the kinetics of protein crystallization at nanometer resolution.[39] This method does not, however, resolve the motion trajectories of single proteins due to the scanning and pushing nature of the probe, and has been limited to crystallization processes on a substrate surface. Cryo-microscopy requires the whole sample solution to be vitrified in the solid state to be imaged in the high vacuum condition of TEM,[40] challenging for resolving either continuous assembly dynamics or the sampling of the free-energy landscape. As a result, theoretical and computational efforts on predicting nanocrystal superlattices have been mostly based on the densest packing structures to favor maximum translational entropy, which can work for anisotropic nanocrystals with dominant entropic forces,[41–43] or the Wulff construction rule,[44] which works for DNA-directed superlattice formation. Both models lack a generic generalizability.

In this article, we review the current status and prospects of another recently emerging technique, liquid cell TEM for studying the nucleation, growth, etching and self-assembly mechanisms of nanocrystals (**Figure 1**), ended with discussion of possible future developments, both technical and conceptual.[45–48] Converse to the archaeologists' strategy of tracing the past from the fossils that survive until now, liquid cell TEM can directly record the past—the temporal series of events in real-space and real-time during synthesis—and measure the crucial kinetic parameters governing this process.

Liquid cell TEM observation of nanocrystal formation and dissolution

Crystallization, including nucleation and growth, is a ubiquitous process for the formation of diverse synthetic and nature materials. From mineralization in organisms, for example, material scientists have been inspired to develop advanced functional materials. Therefore, understanding crystallization is necessary to manipulate structure and morphology of materials on demand. As one of promising analytic methods, liquid cell TEM has provided relevant spatial and temporal resolutions sufficient to capture crystallization phenomena.[45,49–51] Various crystallization events have been directly visualized by tracking distribution of as-formed nanocrystals[52] or their growth trajectories including shape evolution and crystallographic changes.[53] In colloidal nanocrystals, construction of specialized architectures via their growth or etching have been investigated in their native liquid environment.[52–62] In mineralization, furthermore, the debatable part of crystallization, such as growth order of polymorphs[63–65] and preferred nucleation site,[66] have been discussed through solution-mediated precipitation. We introduce outstanding *in situ* microscopic studies which have strengthened theoretical expectation and expanded the possibility of controllable material synthesis.

Revealing crystallization process of metal nanocrystals using liquid cell TEM

In liquid cell TEM studies for crystallization of metal nanoparticles, the electrons necessary for TEM imaging are used to reduce metal ions, driving generation of metal atoms that nucleate and grow into nanocrystals.[67–69] Electron-beam-driven chemical processes share many similarities with conventional wet chemical synthetic processes, because hydrated electrons generated during electron irradiation serve as a reducing agent similar to chemical-reducing agents.[53] However, electron charging, radical species, and changes in the ionic strength

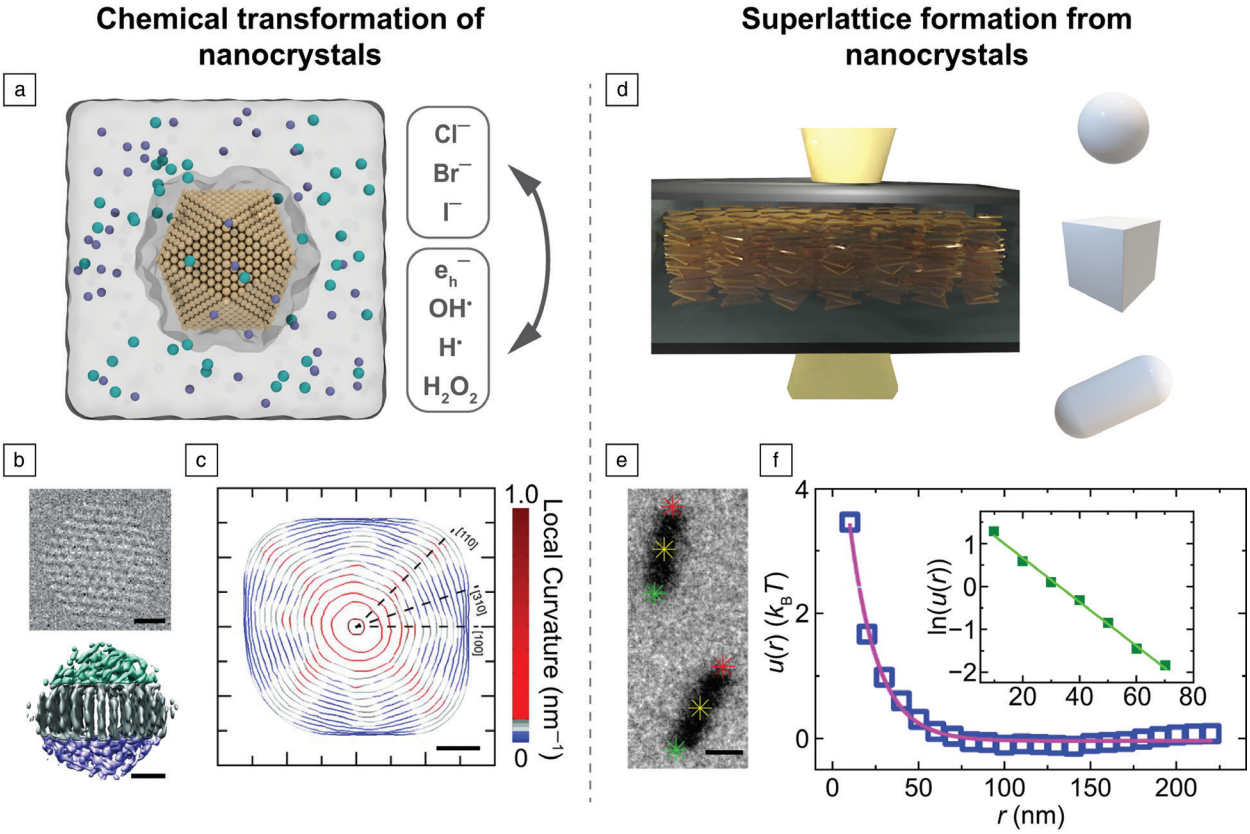

Figure 1. Use of liquid cell transmission electron microscope (TEM) to image and understand chemical transformation (e.g., nucleation, growth, and etching) and assembly into a superlattice of nanocrystals. (a) Schematic of the impact of different species, additives, and the exposure of distinct facets on reaction kinetics. (b) Inferred growth mechanism of platinum nanocrystals (top, TEM) by 3D reconstruction (bottom). Scale bars = 0.5 nm. Reprinted with permission from Reference 46. © 2015 AAAS. (c) Time-domain contour plots showing the etching process of a gold nanocube. Scale bar = 10 nm. Reprinted with permission from Reference 47. © 2016 AAAS. (d) Illustration of liquid cell TEM observations of superlattice formation from nanocrystals. (e) Liquid cell TEM image of two assembling nanorods with their tips (red and green stars) and centroid (yellow stars) position highlighted. Scale bar = 20 nm. (f) Pairwise interaction $u(r)$ between the nanorods shown in (e) extracted from experiments with exponential fitting (red line). The inset shows the exponential decay relation of $u(r)$ by illustrating the linear relationship of $\ln(u(r))$ versus r. Adapted with permission from Reference 48. © 2015 American Chemical Society.

of the solution could lead to minor differences between the electron beam-assisted growth and conventional wet chemistry growth.[68,69] Therefore, it is necessary to understand and manipulate the electron dose conditions in the liquid cells not only for a reasonable interpretation of the beam-initiated growth mechanisms, but also for alleviation of beam-induced artifacts. The article by Woehl et al. in this issue discusses radiation chemistry in detail.[70] Woehl et al. suggested that a certain threshold for electron dose is required to initiate nucleation of nanocrystals, and the electron dose rate influences particle growth behavior (**Figure 2**a–b).[52] Under a high-current beam, for example, metal ions are rapidly exhausted and depletion of metal ions results in diffusion-limited growth of particles. In contrast, under low-current beam, the reduction rate of precursor ions governs particle growth, leading to the so-called reaction-limited growth.

Nucleation is commonly described by CNT in which a nucleus emerges in a single step from supersaturated solution.[71] Although CNT successfully describes various phenomena, nonclassical nucleation models are introduced to account for inconsistencies in crystallization rate.[72,73] These multistep nucleation pathways can be deduced by observing the intermediate phase of the crystallization process. For example, Loh et al. revealed multistep nucleation in noble metal nanocrystal formation.[62] Gold and silver nanocrystals are formed from the supersaturated solution following three distinct steps (Figure 2c). First, the homogenous solution separates into metal-rich and metal-poor liquid phases as attributed to spinodal decomposition.[74] Second, amorphous nanoclusters are formed from the metal-rich phase. Finally, crystalline nanoparticles are evolved from amorphous nanoclusters. Their report demonstrates the applicability of the sequential crystallization pathways described in nonclassical models. However, previous studies have been restricted to resolving the birth of nuclei, from monomers to ordered atomic clusters. Liquid cell TEM still has plenty of room for exploring and resolving the moment of nucleation, possibly aided by computational modeling.

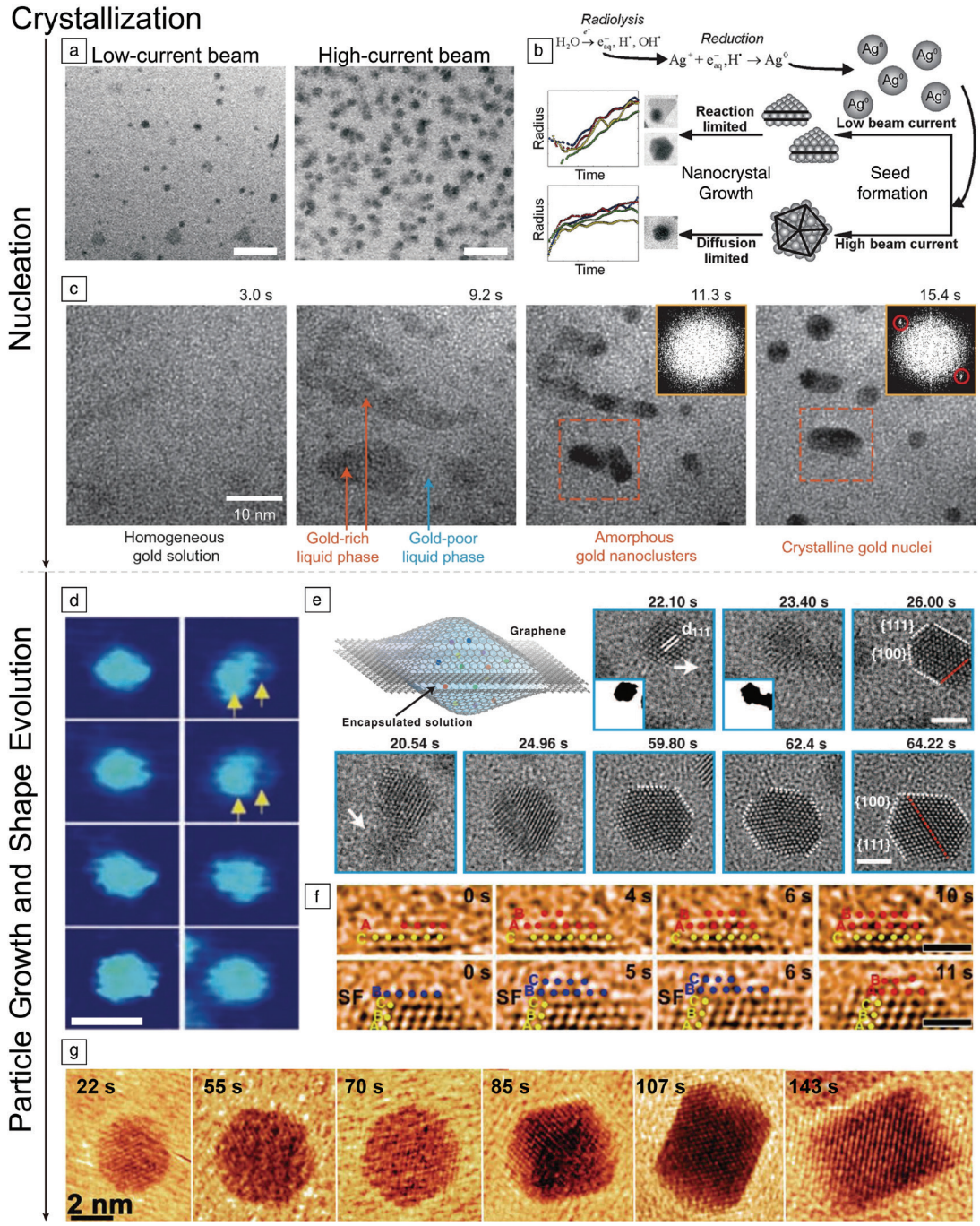

Figure 2. Nucleation and growth of metal nanocrystals observed in liquid cell transmission electron microscopy (TEM). (a) Electron dose-dependent nucleation and growth behavior of silver nanocrystals. The high-current beam produces a larger population of nuclei than the low-current beam. Scale bar = 200 nm. (b) During nanocrystal growth, low beam currents facilitate reaction-limited growth, while higher beam currents promote diffusion-limited growth. (a, b) Reprinted with permission from Reference 52. © 2012 American Chemical Society. (c) Sequential TEM images showing multistep nucleation pathway following spinodal decomposition. Reprinted with permission from Reference 62. © 2016 Springer Nature. (d) Sequential TEM images showing two types of growth mechanism. Both monomer attachment (left column) and coalescence (right column) contribute to crystal growth and lead to identical particle sizes. Scale bar = 5 nm. Reprinted with permission from Reference 53. © 2009 AAAS. (e) Series of sequential atomic-resolution TEM images acquired in graphene liquid cells (schematic illustration). Preferential coalescence along mirror {111} plane results in formation of twin boundary (red dotted line) in hexagonal shape of particles. Scale bar = 2 nm. Reprinted with permission from Reference 58. © 2012 AAAS. (f) Sequential atomic-resolution TEM images showing particle growth by monomer attachment. Platinum atoms exhibit layer-by-layer stacking on {111} surface and stacking faults are annealed around the surface of the nanoparticle. Scale bar = 1 nm. Reprinted with permission from Reference 59. © 2015 American Chemical Society. (g) The facet development of a platinum nanocube during monomer attachment. Reprinted with permission from Reference 57. © 2014 AAAS. Note: PSS, polystyrene sulfonate; NP, nanoparticle.

Liquid cell TEM has also contributed to understanding growth pathways of metal colloidal nanocrystals. Conventionally, the growth process of colloidal nanocrystals has been understood by observing aliquots extracted from samples at different growth stages. Zheng et al. acquired a time series of movies for colloidal platinum growth using SiN_x liquid chips and revealed that nanoparticle growth follows both classical and nonclassical models (Figure 2d).[53] In the classical model, crystallization proceeds by monomer attachment onto preexisting crystals. In the nonclassical model, on the other hand, crystallization occurs through aggregation or coalescence of particles. In this study, some detailed questions of growth dynamics, such as temporary pause of particles right before their merging or defect formation, was not fully understood due to the limited spatial resolution caused by the thick SiN_x viewing window. As an alternative, Yuk et al. developed graphene liquid cells (GLCs) with a single-carbon-atom-thick graphene viewing window that provides atomic-resolution imaging (Figure 2e).[58,75] They discovered that nanocrystals make a narrow neck of a few nanometers length just before their coalescence and that they are fully merged by subsequent surface diffusion of atoms within few seconds.[58] When particles are merged, the grain boundaries are formed at {111} planes with the lowest surface energy. If particles are merged with mirror {111} planes, a twin boundary is formed at the interface and locked in the particle. Using three-dimensional (3D) structure identification of nanocrystals by GLC TEM,[46] it was also observed that twist grain boundaries are formed at interface planes between {110} and {100} planes in which the misalignment angle of {111} planes in each particle is 14°, an angle with the lowest interface energy. These results imply that nanocrystals grown by coalescence could have defects. In the monomer attachment growth mode, however, particles grow layer-by-layer and stacking faults are easily annealed when a stacking sequence is faulted near a surface, resulting in defect-free crystals (Figure 2f).[59]

Liquid cell TEM has been also used to study the evolution of particle shape, which strongly affects their performance in catalysis, sensing, and other surface-mediated applications.[76] The shapes of crystals have been theoretically predicted by the Wulff construction in which high-energy surfaces grow faster than the low-energy surfaces. Consequently, a fast-growing surface eventually disappears, resulting in a nanocrystal terminated with low-energy surfaces. However, Liao et al. demonstrated that the growth of nanocrystals deviates from the surface energy minimization rules (Figure 2g).[57] Because of small differences of nucleation barriers at the nanoscale, three low-energy surfaces, {100}, {110}, and {111}, exhibit similar growth rates until a particle reaches a critical size of ~5 nm. Above this critical size, the final shapes of particles are determined by ligand blocking for atom attachment on a surface. As a result, the less blocked {110} and {111} surfaces continue to grow until the entire shape of a nanocube is formed.

Other nonspherical structures, such as nanowires or nanorods, can be obtained by coalescence events.[55,77] For the coalescence of nanoparticles, interaction between particles includes van der Waals, hydrostatic, or dipolar interaction, and other phenomena that affect growth direction and final morphology of the nanocrystals. For example, Pt-Fe nanoparticles are preferentially aligned along the same direction due to dipolar interaction between particles and attach to the ends of preexisting chains.[54]

Liquid cell TEM has been applied to investigating the mechanism of shape modification in other environmental conditions, such as temperature,[78] precursor concentration,[67] surfactants,[55] and template-mediated synthesis,[79] including heterogeneous nanoparticles.[80,81] Such direct observations of shape evolutions provides a much deeper and richer understanding of generation mechanism of nanoparticles with monodispersed particle size resulting from colloidal synthesis approaches.

Solution-mediated precipitation of salts under liquid cell TEM

In addition to the electron beam-driven growth of nanocrystals, the precipitation of insoluble salts, which is grown by controlling the supersaturation level of aqueous solution, has been studied using liquid cell TEM due to its importance in Nature. However, the highly complex nature of the precipitation environment, such as supersaturation, temperature, pressure, pH, and incorporated additives, has restricted researchers from establishing general rules for controllable synthesis of precipitates.[82–85] To complete the map of precipitation pathways, therefore, it is necessary to track individual growth trajectories, for example, the morphology evolution or the kinetics of intermediate phase transitions. Liu et al. reported the classical growth pathways of $BaWO_4$ crystals in a mixture of Na_2WO_4 and $BaCl_2$ solution using liquid cell TEM (**Figure 3**a).[86] They observed monomer attachment growth at different conditions of supersaturation and ethanol-water ratio, and concluded that the morphology of crystals is determined at the initial stage of the growth, namely, the initial crystal shape is maintained until the end of the growth.

A nonclassical growth mechanism in the precipitation process was also demonstrated by Li and co-workers (Figure 3b).[87] Using a liquid flow cell system, they observed oriented attachment (OA) of iron oxyhydroxide nanoparticles, leading to defect-free or twinned interfaces. OA occurs through diffusion of adjacent particles and their rotation for crystallographic alignment. Thereafter, they attach to each other in a sudden "jump-to-contact" manner. The formation of perfect lattice planes is attributed to the elimination of edge dislocations in the mismatched interface. It was also reported that grains of Na_2SO_4 minerals grow through the grain-boundary migration simultaneously with orientation alignment of the grains (Figure 3c).[60] However, the growth of amorphous calcium carbonate (ACC) occurs via the coalescence process rather than the OA process.

Another nonclassical growth pathway in precipitation, transitional growth involving multiphase polymorphs, was

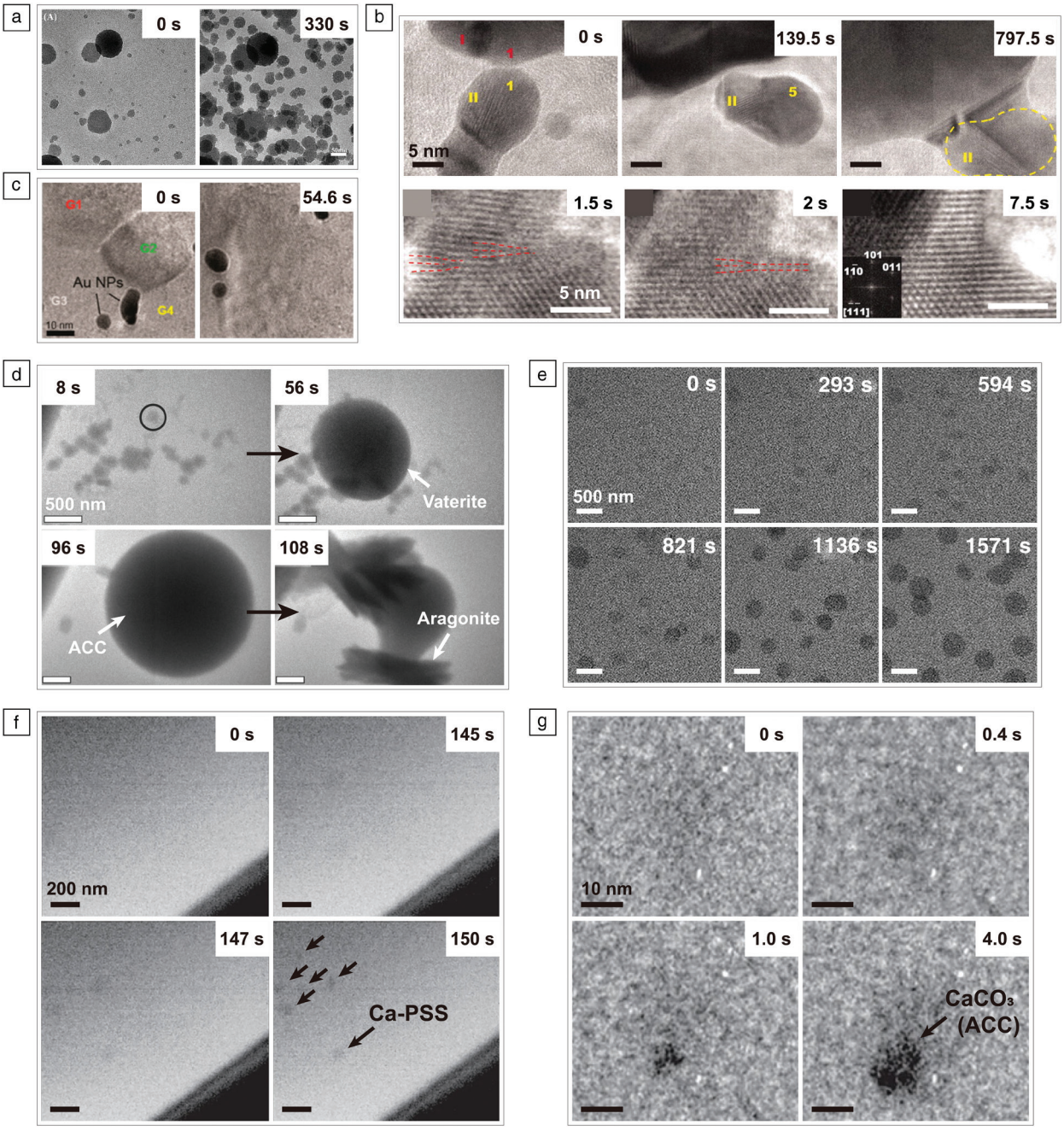

Figure 3. *In situ* liquid cell transmission electron microscope (TEM) studies of the solution-mediated precipitation. (a) Growth of $BaWO_4$ via a classical growth mechanism. Reprinted with permission from Reference 86. © 2018 American Chemical Society. (b) Time-series images in top row showing that the growth of ferrihydrite occurs via oriented attachment. Bottom row shows the formation of single ferrihydrite crystal by elimination of edge dislocations (indicated by the red dashed line). Reprinted with permission from Reference 87. © 2012 AAAS. (c) Grain-boundary migration and grain rotation lead to grain growth of Na_2SO_4, which is revealed by utilizing a graphene liquid cell. Reprinted with permission from Reference 60. © 2016 American Chemical Society. (d) Growth of $CaCO_3$ via multiphase transition. Top row shows direct nucleation of vaterite from solution and bottom row shows indirect nucleation of aragonite on or in the relatively metastable polymorph of amorphous calcium carbonate (ACC). Reprinted with permission from Reference 66. © 2014 AAAS. (e) Growth and phase transformation of ACC without changes of morphology in the presence of Mg ions (5 mM). Reprinted with permission from Reference 88. © 2020 National Academy of Sciences. (f, g) Organic matrix-mediated modification of $CaCO_3$ nucleation. Reprinted with permission from Reference 89. © 2015 Nature Publishing Group. (f) Time-series TEM images showing the formation of hydrated Ca–PSS globules. (g) Formation of an ACC within a Ca-PSS globule after diffusion of ammonium carbonate.

also reported. The occurrence of polymorphism has been explained with Ostwald's rule of stages, which describes the sequential formation of phases from a less stable to a more stable one.[63–65] Using a dual-inlet liquid flowing system, Nielsen et al. directly observed the sequential transformation into more ordered phases (Figure 3d).[66] They demonstrated that the transitional growth of $CaCO_3$ originates from a multiple nucleation pathway, involving direct nucleation from solution and indirect nucleation from metastable phases. Recently, Liu et al. reported a phase transformation from ACC to calcite in the presence of Mg ions (Figure 3e),[88] in which the Mg ions alter the transformation pathway in a concentration-dependent manner. They propose a series of possible mechanisms: (1) Mg ions infuse excess water into the ACC particles. (2) Calcite is subsequently nucleated within the ACC. (3) Finally, ACC is transformed into calcite without any morphological changes. The reported results present a potential method that promises direct phase transformation in the absence of morphological changes.

To obtain polymorphic modifications, it is crucial to establish a complete understanding of the nucleation kinetics, which occurs in the initial stage of the precipitation. In many cases of biomineralization, a hydrated biopolymer matrix alters the nucleation kinetics. Smeets et al. investigated the organic matrix-mediated nucleation pathway of $CaCO_3$ by using the liquid flow cell system (Figure 3f–g).[89] The addition of (polystyrene sulfonate) (PSS) induced the formation of Ca-PSS globules (Figure 3f). Thereafter, ACC nanoparticles were formed on the Ca-PSS globules with diffusion of $(NH_4)_2CO_3$ (Figure 3g). The exclusive formation of ACC within the Ca-PSS complexes implies that the PSS-induced ion binding manipulates the nucleation kinetics of ACC without energy-barrier engineering.

Etching trajectories of nanocrystals

Synthesizing nanomaterials of a desired geometry requires either controllable addition of new atoms to a growing crystal or selective removal of atoms from a larger crystal.[90] Etching is similar to the work of a sculptor, carefully removing unwanted material until the masterpiece is revealed, but traditional etching reactions in a flask provide little information about how the nanocrystals are transformed to the final products. Liquid cell TEM can observe the intermediate shapes of kinetically driven processes without the relaxation challenges associated with quenching techniques, volumetric dissolution rates,[91,92] local etching rates,[93] and the interplay between etching and diffusion.[94] Combining the increased resolution from GLC with the known crystallography and facets of the initial nanocrystals, the intermediate facets during kinetically driven processes can be measured (**Figure 4**a).[95,96] Both gold nanocubes with {100} facets and rhombic dodecahedra with {110} facets transition through {hk0} intermediate facets to a {310} steady facet (Figure 4b).[47] Monte Carlo simulations revealed that the etching trajectories can be reproduced by having the probability of surface atom removal dependent on coordination number. Increasing the chemical potential of the oxidative environment causes an increase in the h/k value of the steady intermediate facet when etching from a cube (Figure 4c),[96] and a change in the facet trajectory but not the steady facet when etching rhombic dodecahedra. The oxidative etching rate of the gold nanocrystals is independently determined by the electron-beam flux (Figure 4d),[97] providing two knobs to separately tune the chemical potential and etching rate in the GLC for controlled etching experiments.

As chemical control and liquid cell design continues to progress, liquid cell etching experiments have extended beyond monometallic systems. Etching bimetallic core–shell nanocubes shows the effect of etching nanocrystals with dissimilar oxidation potentials (Figure 4e). While the cubic Au shell transitions to a tetrahexahedral shape, the corners of the inner Pd cube become exposed. The inner Pd cube begins etching much faster from these exposed edges, leading to a hexapod-like Pd core capped with Au pyramids.[98] Bimetallic systems with a nonnoble metal have even shown dynamics sensitive to whether the etching is chemical or electrochemical.[99] The surface structure of facets can also induce different etching dynamics based on redox conditions, with the relative etching rate of ceria {100} and {111} facets being controlled by the redox potential of the liquid cell.[100]

The mechanisms and intermediate shapes observed during wet chemical etching of semiconductor nanomaterials such as Si[101] and SiGe[102] nanopillars demonstrates how the liquid cell can lead to industrially relevant insights. By fabricating an array of nanopillars, a large number of nanostructures were etched under the same conditions, providing information about the heterogeneity of the system and ensuring reproducibility of the results (Figure 4f). Through continued advancement in liquid cell fabrication and chemical understanding, etching experiments will be able to study more complex materials and architectures while further understanding the effects of chemical influences such as reactants, ligands,[103] and pH.

Superlattice formation from nanocrystals

Nanocrystals have been demonstrated to be greatly versatile artificial atoms that assemble into a huge library of superlattices, including those of complicated unit cells (e.g., clathrates,[104] quasicrystals,[43,105] and binary phases[106,107]), which emulate and sometimes even surpass the diversity of natural atomic solids.[9] The variety and combinations of nanocrystal structural attributes (e.g., size, shape, composition, surface charge, patchiness, and binding energy) are vast, far more extensive than the periodic table.[9,108]

The physical bonds linking nanocrystals into superlattices originate from nanoscale colloidal interactions, which are highly complex due to their long-range and nonadditive nature specific to the nanoscale.[109–111] These interactions can be programmable and can switch in time through variations of extrinsic parameters such as ion concentration, pH, temperature, and the presence of external fields and perturbations (e.g., acoustic, magnetic, and electric). While enriching the dimensionality of

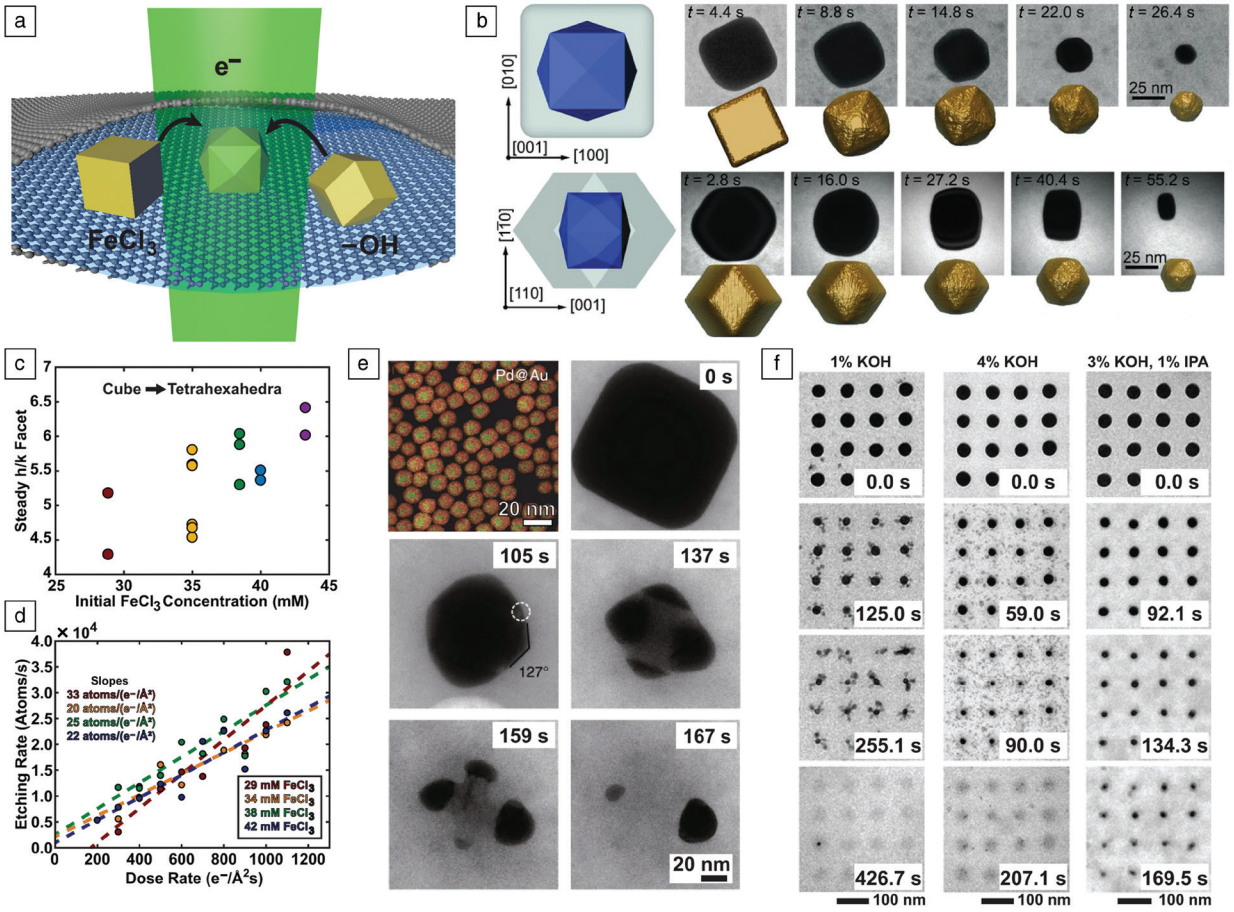

Figure 4. Observing the etching of nanostructures using liquid cell transmission electron microscopy (TEM). (a) Schematic of preformed nanocrystals etched to intermediate shapes in the graphene liquid cell through a combination of electron-beam-induced radiolysis products and preloaded reactants. Reprinted with permission from Reference 96. © 2018 American Chemical Society. (b) Etching a gold cube with {100} facets and a rhombic dodecahedron with {110} facets in a kinetic regime leads to intermediate tetrahexahedra with {hk0} facets. Monte Carlo simulations reproduce the shape transformations as shown by gold polyhedrons beneath the TEM images and reveal surface atom coordination controls the etching trajectory. Reprinted with permission from Reference 47. © 2016 AAAS. (c) Intermediate facets when etching from a cube can be controlled by the etchant chemical potential, here modulated using the initial $FeCl_3$ concentration. Reprinted with permission from Reference 96. © 2018 American Chemical Society. (d) Etching rate can be controlled independently from chemical potential by the electron-beam flux. Reprinted with permission from Reference 97. © 2019 American Chemical Society. (e) Oxidatively etching bimetallic nanocrystals introduces new complexity in the shape trajectory as the two metals etch at different rates due to their oxidation potentials. Adapted with permission from Reference 98. © 2020 Springer Nature. (f) Wet-etching silicon nanowires in the TEM also reveals etch intermediates. Patterning the silicon nanopillars enabled large numbers of controlled nanostructures to be probed in the liquid cell. Adapted with permission from Reference 101. © 2017 American Chemical Society.

design space, this multitude of intrinsic and extrinsic parameters renders it hard to decouple and elucidate the impact of each parameter.[112] Prevalent experimental characterization provides limited insights as discussed in the introduction, and the successes of simulation efforts mostly lie in understanding entropy-driven packing of anisotropic nanocrystals, where only the volume exclusion interaction is considered and the driving force is ascribed to an "entropic patchiness," namely the preferential interaction between planar facets of nanocrystals over the curved surface regions.[113] This concept has been frequently employed to guide experimental efforts to make superlattices from nonpolar, anisotropic nanocrystals where the configurational entropy effects dominate.

Murray and co-workers demonstrated that $NaYF_4$ nanocrystals in the shapes of spheres, rods, hexagonal prisms, and plates self-assemble into densely packed long-range ordered tilings following this entropy effect.[42] Ye et al. showed that similar arguments work for binary nanocrystals where the relative size of gold nanorods and gold nanospheres was varied, generating different types of phases, including lamellar structure with disordered spheres and AB_2-type binary superlattices.[107] Meanwhile, many other nanocrystal systems have more complicated interactions that dominate beyond the entropy effects, such as electrostatic interaction due to the presence of surface charges in polar solvents, where these predictions do not apply.[110]

The extensive efforts in preparing nanocrystal superlattices requires further understanding of the fundamental nucleation and growth pathways as well as the associated free-energy landscape governing the formation and phase behaviors of nanocrystal superlattices, which is still in its infancy. We highlight recent efforts next providing complementary mechanistic insights by liquid cell TEM from *in situ* real-space imaging of the complete crystallization process of superlattices in their native solution state. These experiments are made possible by the community's efforts in understanding and control of the effects of the electron beam, substrate adhesion and confinement in the liquid cell environment, and in advanced data mining based on statistical mechanics principles at the underexplored nanoscale.

One-dimensional chains and 2D nanocrystal superlattice formation under liquid cell TEM

Using liquid cell TEM to study nanocrystal superlattices with global ordering is a recently emerging direction, building upon the extensive liquid cell TEM studies on nanocrystal assembly into small clusters exhibiting disordered structural motifs. Nanocrystals exhibit random Brownian motion when dispersed in solvents, which are transformed into local vibrations composing ordered superlattices. In 2012, Park and co-workers reported the first liquid cell TEM study that captured the formation of a 2D hexagonal superlattice assembled from Pt nanospheres (**Figure 5**b).[114] The first-generation static SiN_x cell was used, which upon electron-beam illumination induces a combination of capillary force and solvent fluctuation to drive a two-step crystallization process. The Pt nanospheres were first concentrated into amorphous agglomerates upon partial solvent drying, which then locally relaxed into crystalline domains.

Further research efforts focused on the crystallization of nanocrystal superlattices driven by the equilibrium nanoscale forces instead of solvent convection, to emulate laboratory-scale solution-phase nanocrystal superlattice growth outside the TEM.[109,115,116] Zheng and co-workers observed the formation of a 2D superlattice assembled from Fe-Pt nanospheres and quantitatively evaluated the contributions of thermal fluctuation, hydrodynamic effects, van der Waals force, and steric hindrance to the crystallization.[115] These nanoscale forces are all physical in nature, highly tunable and reversible, in contrast to covalent bonds.

Similarly, Li and co-workers studied silver nanospheres, and used the fluctuation dissipation theorem to derive a force–distance profile of a pair of interacting nanospheres directly from their measured relative velocity and diffusion coefficient (Figure 5c–d).[115] This profile was then fitted with possible mathematical forms of different forces to elucidate the role of balanced forces for crystallization. Besides spherical

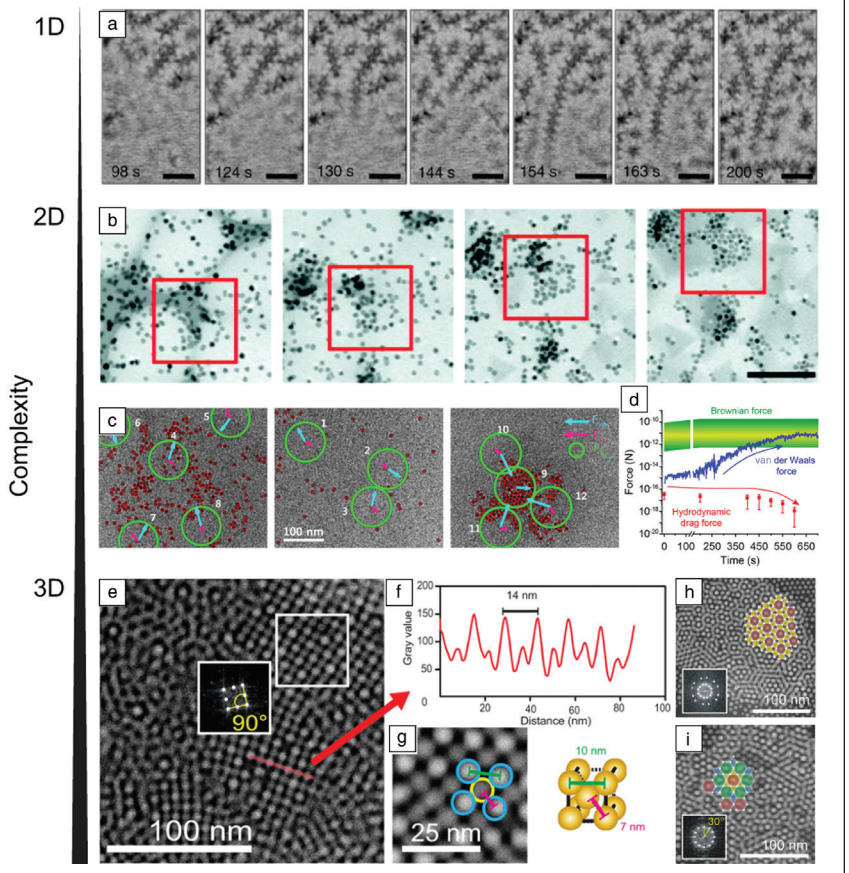

Figure 5. Liquid cell transmission electron microscopy (TEM) studies of nanocrystal superlattices of increasing dimensions. (a) Time-lapse liquid cell TEM images showing the interlocked assembly of 1D superlattice from CdSe/CdS octopods. Reprinted with permission from Reference 117. (b) Time-lapse liquid cell TEM images showing the 2D hexagonal superlattice (regions boxed in red) assembled from Pt nanospheres. Reprinted with permission from Reference 114. © 2012 American Chemical Society. (c) Time-lapse liquid cell TEM images showing 2D hexagonal superlattice assembled from Au nanospheres with the effects from van der Waals attractive force (F_{vdW}, blue arrow), hydrodynamic drag force (F_D, red arrow), and Brownian force (F_{Br}, green circle) labeled in the images. (d) Calculated average F_{vdW}, F_D, and F_{Br} as a function of time. (c, d) Reprinted with permission from Reference 115. © 2018 American Chemical Society. (e–i) Various 3D superlattices assembled from Au nanocrystals observed in liquid cell TEM. Reprinted with permission from Reference 131. © 2020 AAAS. (e) Three-dimensional superlattices formed from overlaid double layers of Au nanocrystals with the corresponding fast Fourier transform (FFT) as the inset. (f) The gray value profile along the red line (noted in [e]) showing the layered feature of the superlattice. (g) Digital zoom-in view of the square region in (e) and its 3D body-centered-cubic structure model. (h, i) Superlattice with a rhombitrihexagonal (h) and quasicrystal (i) pattern assembled from Au nanocrystals.

nanocrystals, which pack almost unanimously into hexagonal lattices in 2D, more recent liquid cell TEM studies have started to investigate effects of anisotropic nanocrystal shapes. For example, CdSe/CdS octopod nanocrystals dispersed in toluene were observed to assemble into a interlocked 1D superlattice (linear chains) under liquid cell (S)TEM, which matches the 1D structural motifs observed outside TEM (Figure 5a).[117] The growth dynamics are consistent with a generic model relating the 1D superlattice to molecular polymerization without including the complications of the electron beam. In these studies where entropy effects alone are not sufficient to explain phase behaviors, one common finding is that the driving forces are drastically controlled by the nanoscopic morphological details of the particles (e.g., local curvature, truncation), which renders the nanometer-resolving capability of liquid cell TEM crucial.[118]

In these studies, the suspension of nanocrystals is kept thin in the liquid cell, slightly more than the thickness of one monolayer of nanocrystals. As a result, the superlattices are mostly 1D (chains) and 2D (monolayers), with limited diffusion (or out-of-focus blurring) of nanocrystals in the vertical direction. This facilitates data mining based on single particle tracking and trajectory analysis at nanometer resolution, such as the application of machine learning method to extract the anisotropic interaction landscape and assembly motifs from liquid phase TEM videos. [119]

Concurrent with these studies are the advancements in understanding the liquid environment inside liquid cell TEM. For most liquid cell TEM studies, the effect of heating[120] or plasmonic force[121,122] induced by the electron beam is negligible. Radiolysis reaction modeling[68] and surveys of experimental results (e.g., the correlative characterization of a 1D nanoprism superlattice by liquid cell TEM and SAXS)[123] show that at low dose rate conditions, the electron beam effectively acts as a steady-state source of ions, which screen electrostatic interactions in solvents. Accordingly, the electron beam can serve both as an imaging probe and an environmental trigger to initiate the formation of nanocrystal superlattices.[124]

Apart from radiolysis, the effect of the encapsulating window membranes in direct contact with the nanocrystal suspension has also caught increasing attention. Characterization of the membranes such as by scanning chemical force microscopy by Woehl and co-workers shows that surface charging and chemical heterogeneity can lead to nanocrystal–substrate attraction.[125] This attraction can be employed to confine the nanocrystal motion to a quasi-2D plane (and thereby induce 1D and 2D crystallization), or act to slow the diffusion of nanocrystals,[126] thereby preventing the formation of large superlattices due to lack of structural rearrangement to escape from kinetic traps.

Three-dimensional layered superlattice and nonclassical crystallization pathways

While CNT theories provide a concrete framework to model behaviors, where a nucleus fluctuates until it overcomes a critical size, converse nonclassical crystallization pathways have recently been found in various synthetic, biogenic, and geologic environments. Nonclassical crystallization pathways encompass many processes, as long as the crystallization goes beyond monomer addition, from prenucleation precursors, OA to coalescence, which pinpoints the critical role of kinetic pathways in defining the crystal habit of final crystal.[71] Liquid cell TEM studies of 1D and 2D superlattices suggested the presence of nonclassical crystallization pathways to some extent though the concept was not vigorously tested.[114,116] The two studies described next on 3D nanocrystal superlattices, instead, have explicitly analyzed complex structural evolutions during crystallization.

Luijten, Chen and co-workers captured the complete nonclassical crystallization in a 3D nanocrystal superlattice using liquid cell TEM of a thick liquid sample that accommodates multiple layers of nanocrystals.[124] The system is comprised of anisotropic gold triangular nanoprisms coated with negatively charged carboxylate ligands, which provide electrostatic repulsion in water. As the ion concentration increases, van der Waals attraction between the prisms overrun electrostatic repulsion to drive the prisms to stack face-to-face into cylindrical columns standing on the membrane. The columns interact laterally to assemble into a hexagonal columnar superlattice (**Figure 6**a). The global order of the superlattice extends over areas of μm^2, which was made possible by meticulous screening of nanocrystal–substrate attraction. In doing so, the nanocrystals diffuse fast, not bounded by the substrate, allowing for rearrangement and self-correction of mispositioned nanocrystals into a large-scale superlattice. To ensure a high concentration of nanoprisms in the liquid cell, highly concentrated preassembled prisms were first loaded into the liquid cell and then disassembled into individual prisms "on spot" by solvent exchange enabled by flow liquid cells. This high initial concentration of nanocrystals helps control supersaturation in the 3D solution volume once crystallization is triggered, to maximally represent experiments outside TEM.

The dynamic movies obtained in this work include numerous local and transient events of restructuring and annealing, which serve as a potent data set allowing the implementation of statistical mechanics analysis to map a complete crystallization coordinate and free-energy landscape. This workflow has been used before in analyzing optical microscopy movies of micron-sized colloids,[127] and its applicability to liquid cell TEM studies highlights the highly quantitative experimental control of the liquid cell environment that is central to minimally invasive imaging of the phase behaviors at the nanoscale. As shown in Figure 6b–c, the positions of individual nanocrystals were first tracked, from which local structural order parameters such as the bond orientational order parameter and local density—the most relevant in the hexagonal columnar lattice—were computed at the single nanocrystal level.[124] In doing so, the TEM movies were digitally translated into matrices

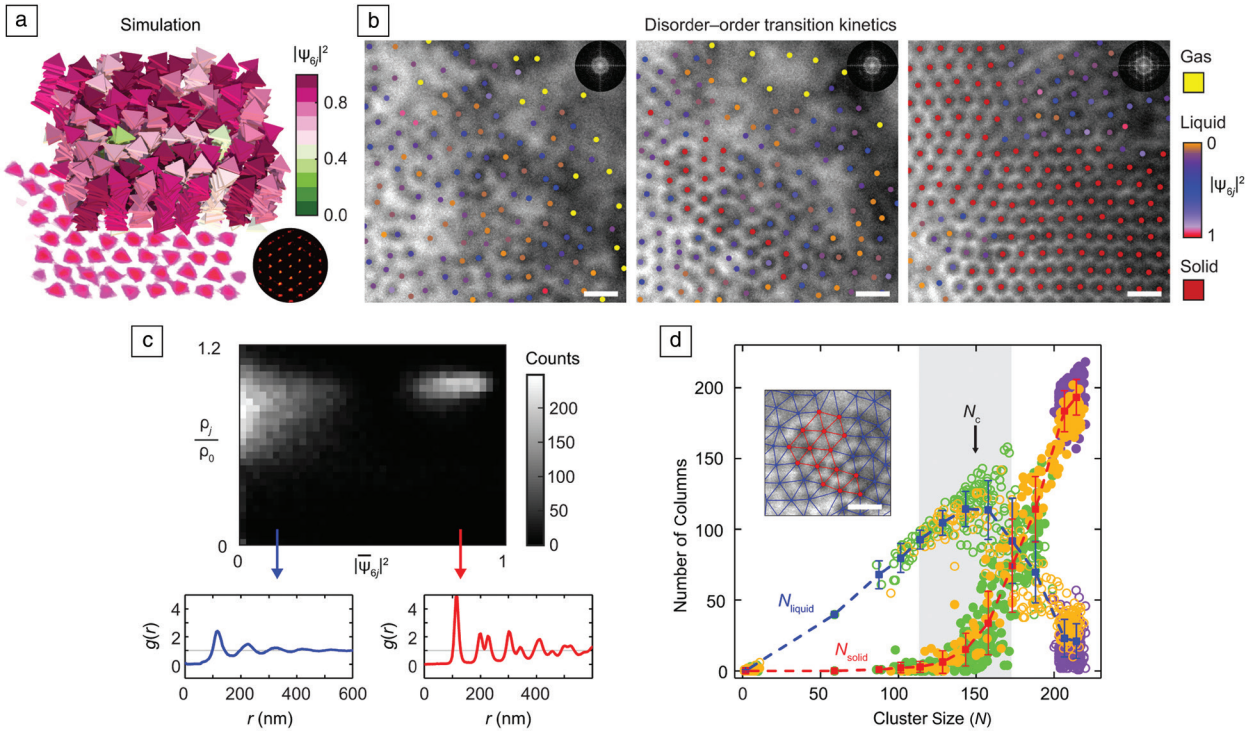

Figure 6. Nonclassical crystallization pathway in a 3D nanocrystal superlattice mapped by liquid cell transmission electron microscopy (TEM). (a) Illustration of the 3D hexagonal columnar superlattice formed by triangular nanoprisms. (b) Time-lapse TEM images with individual columns colored to different local ordering showing the real-time nonclassical crystallization process. (c) The local order-density histogram highlighting the two most stable states. (d) Temporal evolutions of the amorphous intermediate (blue) and the final crystallite (red) populations. Inset: TEM image showing the wetting of the amorphous layer. Scale bars = 200 nm. Reprinted with permission from Reference 124. © 2019 Springer Nature.

of parameters monitoring the sampling of free-energy landscape by the nanocrystals.

The derived 2D local order-density histogram shows two most probable structural states (Figure 6c) following Boltzmann distribution in equilibrium: nanocrystals tend to dwell longer and more frequently at the lower free energy states. One of the most probable states marks an amorphous intermediate as prenucleation precursor, from which embryos of ordered crystallites subsequently nucleate and grow. The energetic origin of the intermediate can be attributed to a competition between interfacial energy and chemical potential, which has also been used to explain two-step solid–solid phase transition in micron-sized colloidal systems.[128] By forming an amorphous phase to wet the interface of the solid nucleus and the disordered suspension, the barrier for nucleation is lowered (Figure 6d), which was measured by tracking the number distribution of clusters. This methodology of mapping the intermediate structures together with thermodynamic properties can potentially be extended to investigate the complicated energy landscapes in other superlattices, and even the transformation of biological molecules, such as protein folding[129] and DNA condensation.[130]

While the previously discussed work presented a remarkable nonclassical crystallization pathway to a straightforward 3D superlattice structure, de Jonge and co-workers in recent work developed protocols to fine-tune the substrate–nanocrystal interaction and harnessed a diversity of 3D layered superlattices assembled from oleyamine-coated gold nanocrystals at the solid (SiN_x membrane)–liquid interface in liquid cell (S)TEM (Figure 5e–i).[131] In this layered assembly, dense packings of hexagonal symmetry were observed for the first monolayer on the membrane regardless of the solvent type. On top of this layer, a second layer was further grown (Figure 5e–g). Depending on the strength of the substrate–nanocrystal interaction, the second layer exhibited rich geometries ranging from dense packing, which leads to various Moiré patterns depending on its orientation relative to the first layer, to a quasicrystal—a first time realization in liquid cells (Figure 5h–i). The exquisite control achieved in this work suggests an exciting future for nanocrystal superlattice crystallization studies in liquid cells, to fully explore and understand the underlying mechanisms as now one can potentially realize equivalents of laboratory-scale systems outside the TEM.

Conclusions

The enormous efforts in using liquid cell EM to understand nanocrystal formation and superlattice assembly has injected

new insights into many materials science fields. For example, observing these processes in situ reveals remarkable parallels between atoms forming into nanocrystals and nanocrystals assembling into superlattices, such as nonclassical crystallization. This convergence across length scales can inspire us to adopt the theories and strategies from nanocrystal synthesis, such as seeded growth, anisotropic growth rates modulated by additives, and lattice mismatch induced patch formation, for making nanocrystal superlattices of exotic morphologies that are otherwise inaccessible.

Meanwhile, the advent of fast TEM detectors capable of capturing hundreds to thousands of frames per second[57,132] can make it possible to investigate and image systems at lower dose rates for beam sensitive samples (e.g., unstable nanocrystals, proteins, cells, polymers) or low-radiolysis environments. The rapid camera rate also provides the opportunity to capture fast processes such as nanoscale diffusion, catalytic reactions, protein folding, and biological recognition. The generation of large data sets demands new data infrastructure and advanced datamining techniques such as machine learning to extract physical parameters automatically from liquid-phase TEM movies.

Incorporation of artificial intelligence into smart, automated, and remote operation of electron microscopes to match the greatly increased volume of spatiotemporal data collected by liquid cell TEM will increase the quality and quantity of *in situ* data. While current liquid cell TEM operation protocols are mature for resolving the projected, 2D morphology of nanosized entities, they can be coupled with other frontier electron microscopy methods,[133] such as electron tomography, composition mapping, electron holography,[134] to push the dimensionality of information collected for more complex materials. The ability to observe nanoscale process in their liquid environment has already had a significant impact on the understanding of nanocrystal formation and superlattice assembly, and new advances in equipment and experimental technique will further deepen our knowledge of nanoscale dynamics.

Acknowledgments

Q.C. was supported by the National Science Foundation through Award No. DMR-1752517. J.M.Y. was supported by the National Research Foundation of Korea (NRF) grant funded by the Korean government (MSIP; Ministry of Science, ICT & Future Planning) (NRF-2018R1C1B6002624). A.P.A. was supported by the US Department of Energy, Office of Science, Office of Basic Energy Sciences, Materials Sciences and Engineering Division, under Contract No. DE-AC02-05-CH11231 within the Physical Chemistry of Inorganic Nanostructures Program (KC3103).

References

1. Y. Xia, Y. Xiong, B. Lim, S.E. Skrabalak, *Angew. Chem. Int. Ed. Engl.* **48**, 60 (2009).
2. L.M. Liz-Marzán, *Mater. Today* **7**, 26 (2004).
3. C.J. Murphy, T.K. Sau, A.M. Gole, C.J. Orendorff, J. Gao, L. Gou, S.E. Hunyadi, T. Li, *J. Phys. Chem. B* **109**, 13857 (2005).
4. G. Wang, Q. Peng, Y. Li, *Acc. Chem. Res.* **44**, 322 (2011).
5. J. Gao, H. Gu, B. Xu, *Acc. Chem. Res.* **42**, 1097 (2009).
6. S. Sun, H. Zeng, *J. Am. Chem. Soc.* **124**, 8204 (2002).
7. A.M. Smith, S. Nie, *Acc. Chem. Res.* **43**, 190 (2010).
8. C.P. Collier, T. Vossmeyer, J.R. Heath, *Annu. Rev. Phys. Chem.* **49**, 371 (1998).
9. M.A. Boles, M. Engel, D.V. Talapin, *Chem. Rev.* **116**, 11220 (2016).
10. T. Wang, D. LaMontagne, J. Lynch, J. Zhuang, Y.C. Cao, *Chem. Soc. Rev.* **42**, 2804 (2013).
11. X. Yang, M. Yang, B. Pang, M. Vara, Y. Xia, *Chem. Rev.* **115**, 10410 (2015).
12. Z. Li, Q. Sun, Y. Zhu, B. Tan, Z.P. Xu, S.X. Dou, *J. Mater. Chem. B* **2**, 2793 (2014).
13. E.C. Dreaden, A.M. Alkilany, X. Huang, C.J. Murphy, M.A. El-Sayed, *Chem. Soc. Rev.* **41**, 2740 (2012).
14. Y.C. Cao, R. Jin, C.A. Mirkin, *Science* **297**, 1536 (2002).
15. K.M. Mayer, J.H. Hafner, *Chem. Rev.* **111**, 3828 (2011).
16. G. Konstantatos, E.H. Sargent, *Nat. Nanotechnol.* **5**, 391 (2010).
17. S. Ye, A.R. Rathmell, Z. Chen, I.E. Stewart, B.J. Wiley, *Adv. Mater.* **26**, 6670 (2014).
18. S. Lal, S. Link, N.J. Halas, *Nat. Photonics* **1**, 641 (2007).
19. Y. Geng, G. van Anders, P.M. Dodd, J. Dshemuchadse, S.C. Glotzer, *Sci. Adv.* **5**, eaaw0514 (2019).
20. D. Morphew, J. Shaw, C. Avins, D. Chakrabarti, *ACS Nano* **12**, 2355 (2018).
21. Z. Jia, F. Liu, X. Jiang, L. Wang, *J. Appl. Phys.* **127**, 150901 (2020).
22. J. Nai, S. Wang, X.W.D. Lou, *Sci. Adv.* **5**, eaax5095 (2019).
23. M. Kadic, G.W. Milton, M. van Hecke, M. Wegener, *Nat. Rev. Phys.* **1**, 198 (2019).
24. T.-H. Yang, Y. Shi, A. Janssen, Y. Xia, *Angew. Chem. Int. Ed. Engl.* (2019), doi:10.1002/anie.201911135.
25. G. Krylova, L.J. Giovanetti, F.G. Requejo, N.M. Dimitrijevic, A. Prakapenka, E.V. Shevchenko, *J. Am. Chem. Soc.* **134**, 4384 (2012).
26. J.E. Halpert, V.J. Porter, J.P. Zimmer, M.G. Bawendi, *J. Am. Chem. Soc.* **128**, 12590 (2006).
27. T. Mokari, C.G. Sztrum, A. Salant, E. Rabani, U. Banin, *Nat. Mater.* **4**, 855 (2005).
28. V. Mazumder, M. Chi, K.L. More, S. Sun, *Angew. Chem. Int. Ed. Engl.* **49**, 9368 (2010).
29. T. Mokari, E. Rothenberg, I. Popov, R. Costi, U. Banin, *Science* **304**, 1787 (2004).
30. Y. Xia, K.D. Gilroy, H.-C. Peng, X. Xia, *Angew. Chem. Int. Ed. Engl.* **56**, 60 (2017).
31. C. Wang, H. Daimon, S. Sun, *Nano Lett.* **9**, 1493 (2009).
32. M. Guix, S.M. Weiz, O.G. Schmidt, M. Medina-Sánchez, *Part. Part. Syst. Charact.* **35**, 1700382 (2018).
33. S.G. Kwon, G. Krylova, P.J. Phillips, R.F. Klie, S. Chattopadhyay, T. Shibata, E.E. Bunel, Y. Liu, V.B. Prakapenka, B. Lee, E.V. Shevchenko, *Nat. Mater.* **14**, 215 (2015).
34. R.J. Macfarlane, B. Lee, M.R. Jones, N. Harris, G.C. Schatz, C.A. Mirkin, *Science* **334**, 204 (2011).
35. L. Wu, J.J. Willis, I.S. McKay, B.T. Diroll, J. Qin, M. Cargnello, C.J. Tassone, *Nature* **548**, 197 (2017).
36. M.C. Weidman, D.-M. Smilgies, W.A. Tisdale, *Nat. Mater.* **15**, 775 (2016).
37. J.J. Geuchies, C. van Overbeek, W.H. Evers, B. Goris, A. de Backer, A.P. Gantapara, F.T. Rabouw, J. Hilhorst, J.L. Peters, O. Konovalov, A.V. Petukhov, M. Dijkstra, L.D.A. Siebbeles, S. van Aert, S. Bals, D. Vanmaekelbergh, *Nat. Mater.* **15**, 1248 (2016).
38. L. Wu, X. Wang, G. Wang, G. Chen, *Nat. Commun.* **9**, 1335 (2018).
39. J.J. De Yoreo, S. Chung, R.W. Friddle, *Adv. Funct. Mater.* **23**, 2525 (2013).
40. G. Mirabello, A. Ianiro, P.H.H. Bomans, T. Yoda, A. Arakaki, H. Friedrich, G. de With, N.A.J.M. Sommerdijk, *Nat. Mater.* **19**, 391 (2020).
41. P.F. Damasceno, M. Engel, S.C. Glotzer, *Science* **337**, 453 (2012).
42. X. Ye, J.E. Collins, Y. Kang, J. Chen, D.T.N. Chen, A.G. Yodh, C.B. Murray, *Proc. Natl. Acad. Sci. U.S.A.* **107**, 22430 (2010).
43. D.V. Talapin, E.V. Shevchenko, M.I. Bodnarchuk, X. Ye, J. Chen, C.B. Murray, *Nature* **461**, 964 (2009).
44. E. Auyeung, T.I.N.G. Li, A.J. Senesi, A.L. Schmucker, B.C. Pals, M.O. de La Cruz, C.A. Mirkin, *Nature* **505**, 73 (2014).
45. F.M. Ross, *Science* **350**, aaa9886 (2015).
46. J. Park, H. Elmlund, P. Ercius, J.M. Yuk, D.T. Limmer, Q. Chen, K. Kim, S.H. Han, D.A. Weitz, A. Zettl, A.P. Alivisatos, *Science* **349**, 290 (2015).
47. X. Ye, M.R. Jones, L.B. Frechette, Q. Chen, A.S. Powers, P. Ercius, G. Dunn, G.M. Rotskoff, S.C. Nguyen, V.P. Adiga, A. Zettl, E. Rabani, P.L. Geissler, A.P. Alivisatos, *Science* **354**, 874 (2016).

48. Q. Chen, H. Cho, K. Manthiram, M. Yoshida, X. Ye, A.P. Alivisatos, *ACS Cent. Sci.* **1**, 33 (2015).
49. M.J. Williamson, R.M. Tromp, P.M. Vereecken, R. Hull, F.M. Ross, *Nat. Mater.* **2**, 532 (2003).
50. A. Radisic, P.M. Vereecken, J.B. Hannon, P.C. Searson, F.M. Ross, *Nano Lett.* **6**, 238 (2006).
51. N. de Jonge, F.M. Ross, *Nat. Nanotechnol.* **6**, 695 (2011).
52. T.J. Woehl, J.E. Evans, I. Arslan, W.D. Ristenpart, N.D. Browning, *ACS Nano* **6**, 8599 (2012).
53. H. Zheng, R.K. Smith, Y.-W. Jun, C. Kisielowski, U. Dahmen, A.P. Alivisatos, *Science* **324**, 1309 (2009).
54. H.-G. Liao, L. Cui, S. Whitelam, H. Zheng, *Science* **336**, 1011 (2012).
55. H.-G. Liao, H. Zheng, *J. Am. Chem. Soc.* **135**, 5038 (2013).
56. H.-G. Liao, K. Niu, H. Zheng, *Chem. Commun.* **49**, 11720 (2013).
57. H.-G. Liao, D. Zherebetskyy, H. Xin, C. Czarnik, P. Ercius, H. Elmlund, M. Pan, L.-W. Wang, H. Zheng, *Science* **345**, 916 (2014).
58. J.M. Yuk, J. Park, P. Ercius, K. Kim, D.J. Hellebusch, M.F. Crommie, J.Y. Lee, A. Zettl, A.P. Alivisatos, *Science* **336**, 61 (2012).
59. M. Jeong, J.M. Yuk, J.Y. Lee, *Chem. Mater.* **27**, 3200 (2015).
60. J.M. Yuk, Q. Zhou, J. Chang, P. Ercius, A.P. Alivisatos, A. Zettl, *ACS Nano* **10**, 88 (2016).
61. S.Y. Kim, K.S. Dae, K. Koo, D. Kim, J. Park, J.M. Yuk, *Phys. Status Solidi A* **216**, 1800949 (2019).
62. N.D. Loh, S. Sen, M. Bosman, S.F. Tan, J. Zhong, C.A. Nijhuis, P. Král, P. Matsudaira, U. Mirsaidov, *Nat. Chem.* **9**, 77 (2017).
63. J.C. Burley, M.J. Duer, R.S. Stein, R.M. Vrcelj, *Eur. J. Pharm. Sci.* **31**, 271 (2007).
64. D.S. Sake Gowda, R. Rudman, *J. Phys. Chem.* **86**, 4356 (1982).
65. G.T. Rengarajan, D. Enke, M. Steinhart, M. Beiner, *Phys. Chem. Chem. Phys.* **13**, 21367 (2011).
66. M.H. Nielsen, S. Aloni, J.J. De Yoreo, *Science* **345**, 1158 (2014).
67. J.E. Evans, K.L. Jungjohann, N.D. Browning, I. Arslan, *Nano Lett.* **11**, 2809 (2011).
68. N.M. Schneider, M.M. Norton, B.J. Mendel, J.M. Grogan, F.M. Ross, H.H. Bau, *J. Phys. Chem. C* **118**, 22373 (2014).
69. J.M. Grogan, N.M. Schneider, F.M. Ross, H.H. Bau, *Nano Lett.* **14**, 359 (2014).
70. T.J. Woehl, T. Moser, J.E. Evans, F.M. Ross, *MRS Bull.* **45** (9), 746 (2020).
71. J.J. De Yoreo, P.U.P.A. Gilbert, N.A.J.M. Sommerdijk, R.L. Penn, S. Whitelam, D. Joester, H. Zhang, J.D. Rimer, A. Navrotsky, J.F. Banfield, A.F. Wallace, F.M. Michel, F.C. Meldrum, H. Cölfen, P.M. Dove, *Science* **349**, aaa6760 (2015).
72. P.G. Vekilov, *Nanoscale* **2**, 2346 (2010).
73. J. De Yoreo, *Nat. Mater.* **12**, 284 (2013).
74. J.W. Cahn, J.E. Hilliard, *J. Chem. Phys.* **31**, 688 (1959).
75. J.M. Yuk, K. Kim, B. Alemán, W. Regan, J.H. Ryu, J. Park, P. Ercius, H.M. Lee, A.P. Alivisatos, M.F. Crommie, J.Y. Lee, A. Zettl, *Nano Lett.* **11**, 3290 (2011).
76. M.-C. Daniel, D. Astruc, *Chem. Rev.* **104**, 293 (2004).
77. G. Zhu, Y. Jiang, F. Lin, H. Zhang, C. Jin, J. Yuan, D. Yang, Z. Zhang, *Chem. Commun.* **50**, 9447 (2014).
78. H.L. Xin, H. Zheng, *Nano Lett.* **12**, 1470 (2012).
79. L.R. Parent, D.B. Robinson, T.J. Woehl, W.D. Ristenpart, J.E. Evans, N.D. Browning, I. Arslan, *ACS Nano* **6**, 3589 (2012).
80. K.L. Jungjohann, S. Bliznakov, P.W. Sutter, E.A. Stach, E.A. Sutter, *Nano Lett.* **13**, 2964 (2013).
81. E. Sutter, K. Jungjohann, S. Bliznakov, A. Courty, E. Maisonhaute, S. Tenney, P. Sutter, *Nat. Commun.* **5**, 4946 (2014).
82. R.-Q. Song, H. Cölfen, *CrystEngComm* **13**, 1249 (2011).
83. Y.S. Han, G. Hadiko, M. Fuji, M. Takahashi, *J. Cryst. Growth* **289**, 269 (2006).
84. Y.-B. Hu, M. Wolthers, D.A. Wolf-Gladrow, G. Nehrke, *Cryst. Growth Des.* **15**, 1596 (2015).
85. D.B. Trushina, T.V. Bukreeva, M.N. Antipina, *Cryst. Growth Des.* **16**, 1311 (2016).
86. L. Liu, S. Zhang, M.E. Bowden, J. Chaudhuri, J.J. De Yoreo, *Cryst. Growth Des.* **18**, 1367 (2018).
87. D. Li, M.H. Nielsen, J.R.I. Lee, C. Frandsen, J.F. Banfield, J.J. De Yoreo, *Science* **336**, 1014 (2012).
88. Z. Liu, Z. Zhang, Z. Wang, B. Jin, D. Li, J. Tao, R. Tang, J.J. de Yoreo, *Proc. Natl. Acad. Sci. U.S.A.* **117**, 3397 (2020).
89. P.J.M. Smeets, K.R. Cho, R.G.E. Kempen, N.A.J.M. Sommerdijk, J.J. De Yoreo, *Nat. Mater.* **14**, 394 (2015).
90. A. Ruditskiy, Y. Xia, *ACS Nano* **11**, 23 (2017).
91. Y. Jiang, G. Zhu, F. Lin, H. Zhang, C. Jin, J. Yuan, D. Yang, Z. Zhang, *Nano Lett.* **14**, 3761 (2014).
92. Y. Jiang, G. Zhu, G. Dong, F. Lin, H. Zhang, J. Yuan, Z. Zhang, C. Jin, *Micron.* **97**, 22 (2017).
93. J. Wu, W. Gao, H. Yang, J.-M. Zuo, *ACS Nano* **11**, 1696 (2017).
94. W. Gao, Y. Hou, Z.D. Hood, X. Wang, K. More, R. Wu, Y. Xia, X. Pan, M. Chi, *Nano Lett.* **18**, 7004 (2018).
95. M.R. Hauwiller, J.C. Ondry, A.P. Alivisatos, *J. Vis. Exp.* **2018**, e57665 (2018).
96. M.R. Hauwiller, L.B. Frechette, M.R. Jones, J.C. Ondry, G.M. Rotskoff, P. Geissler, A.P. Alivisatos, *Nano Lett.* **18**, 5731 (2018).
97. M.R. Hauwiller, J.C. Ondry, C.M. Chan, P. Khandekar, J. Yu, A.P. Alivisatos, *J. Am. Chem. Soc.* **141**, 4428 (2019).
98. L. Chen, A. Leonardi, J. Chen, M. Cao, N. Li, D. Su, Q. Zhang, M. Engel, X. Ye, *Nat. Commun.* **11**, 3041 (2020).
99. S.F. Tan, S.W. Chee, Z. Baraissov, H. Jin, T.L. Tan, U. Mirsaidov, *J. Phys. Chem. Lett.* **10**, 6090 (2019).
100. J. Sung, B.K. Choi, B. Kim, B.H. Kim, J. Kim, D. Lee, S. Kim, K. Kang, T. Hyeon, J. Park, *J. Am. Chem. Soc.* **141**, 18395 (2019).
101. Z. Aabdin, X.M. Xu, S. Sen, U. Anand, P. Král, F. Holsteyns, U. Mirsaidov, *Nano Lett.* **17**, 2953 (2017).
102. Z. Baraissov, A. Pacco, S. Koneti, G. Bisht, F. Panciera, F. Holsteyns, U. Mirsaidov, *ACS Appl. Mater. Interfaces* **11**, 36839 (2019).
103. R. Hufschmid, E. Teeman, B.L. Mehdi, K.M. Krishnan, N.D. Browning, *Nanoscale* **11**, 13098 (2019).
104. H. Lin, S. Lee, L. Sun, M. Spellings, M. Engel, S.C. Glotzer, C.A. Mirkin, *Science* **355**, 931 (2017).
105. X. Ye, J. Chen, M.E. Irrgang, M. Engel, A. Dong, S.C. Glotzer, C.B. Murray, *Nat. Mater.* **16**, 214 (2017).
106. M.A. Boles, D.V. Talapin, *J. Am. Chem. Soc.* **137**, 4494 (2015).
107. X. Ye, J.A. Millan, M. Engel, J. Chen, B.T. Diroll, S.C. Glotzer, C.B. Murray, *Nano Lett.* **13**, 4980 (2013).
108. K.J.M. Bishop, C.E. Wilmer, S. Soh, B.A. Grzybowski, *Small* **5**, 1600 (2009).
109. J. Lee, E. Nakouzi, D. Xiao, Z. Wu, M. Song, C. Ophus, J. Chun, D. Li, *Small* **15**, 1901966 (2019).
110. C.A.S. Batista, R.G. Larson, N.A. Kotov, *Science* **350**, 1242477 (2015).
111. R.H. French, V.A. Parsegian, R. Podgornik, R.F. Rajter, A. Jagota, J. Luo, D. Asthagiri, M.K. Chaudhury, Y.-M. Chiang, S. Granick, S. Kalinin, M. Kardar, R. Kjellander, D.C. Langreth, J. Lewis, S. Lustig, D. Wesolowski, J.S. Wettlaufer, W.-Y. Ching, M. Finnis, F. Houlihan, O.A. von Lilienfeld, C.J. van Oss, T. Zemb, *Rev. Mod. Phys.* **82**, 1887 (2010).
112. Z. Ou, A. Kim, W. Huang, P.V. Braun, X. Li, Q. Chen, *Curr. Opin. Solid State Mater. Sci.* **23**, 41 (2019).
113. E.S. Harper, G. van Anders, S.C. Glotzer, *Proc. Natl. Acad. Sci. U.S.A.* **116**, 16703 (2019).
114. J. Park, H. Zheng, W.C. Lee, P.L. Geissler, E. Rabani, A.P. Alivisatos, *ACS Nano* **6**, 2078 (2012).
115. J. Lee, E. Nakouzi, M. Song, B. Wang, J. Chun, D. Li, *ACS Nano* **12**, 12778 (2018).
116. A.S. Powers, H.-G. Liao, S.N. Raja, N.D. Bronstein, A.P. Alivisatos, H. Zheng, *Nano Lett.* **17**, 15 (2017).
117. E. Sutter, P. Sutter, A.V. Tkachenko, R. Krahne, J. de Graaf, M. Arciniegas, L. Manna, *Nat. Commun.* **7**, 11213 (2016).
118. J. Kim, Z. Ou, M.R. Jones, X. Song, Q. Chen, *Nat. Commun.* **8**, 761 (2017).
119. L. Yao, Z. Ou, B. Luo, C. Xu, Q. Chen, *ACS Cent. Sci.* (2020), doi:10.1021/acscentsci.0c00430.
120. H. Zheng, S.A. Claridge, A.M. Minor, A.P. Alivisatos, U. Dahmen, *Nano Lett.* **9**, 2460 (2009).
121. P.E. Batson, A. Reyes-Coronado, R.G. Barrera, A. Rivacoba, P.M. Echenique, J. Aizpurua, *Nano Lett.* **11**, 3388 (2011).
122. H. Zheng, U.M. Mirsaidov, L.-W. Wang, P. Matsudaira, *Nano Lett.* **12**, 5644 (2012).
123. J. Kim, M.R. Jones, Z. Ou, Q. Chen, *ACS Nano* **10**, 9801 (2016).
124. Z. Ou, Z. Wang, B. Luo, E. Luijten, Q. Chen, *Nat. Mater.* **19**, 450 (2020).
125. M. Wang, T.U. Dissanayake, C. Park, K. Gaskell, T.J. Woehl, *J. Am. Chem. Soc.* **141**, 13516 (2019).
126. C. Liu, Z. Ou, F. Guo, B. Luo, W. Chen, L. Qi, Q. Chen, *J. Am. Chem. Soc.* **142**, 11669 (2020).
127. J.C. Crocker, D.G. Grier, *J. Colloid Interface Sci.* **179**, 298 (1996).
128. Y. Peng, F. Wang, Z. Wang, A.M. Alsayed, Z. Zhang, A.G. Yodh, Y. Han, *Nat. Mater.* **14**, 101 (2015).
129. M. Gruebele, K. Dave, S. Sukenik, *Annu. Rev. Biophys.* **45**, 233 (2016).
130. V.B. Teif, K. Bohinc, *Prog. Biophys. Mol. Biol.* **105**, 208 (2011).
131. E. Cepeda-Perez, D. Doblas, T. Kraus, N. de Jonge, *Sci. Adv.* **6**, eaba1404 (2020).
132. S.W. Chee, U. Anand, G. Bisht, S.F. Tan, U. Mirsaidov, *Nano Lett.* **19**, 2871 (2019).
133. N. de Jonge, L. Houben, R.E. Dunin-Borkowski, F.M. Ross, *Nat. Rev. Mater.* **4**, 61 (2019).
134. M.N. Yesibolati, S. Laganà, H. Sun, M. Beleggia, S.M. Kathmann, T. Kasama, K. Mølhave, *Phys. Rev. Lett.* **124**, 065502 (2020). □

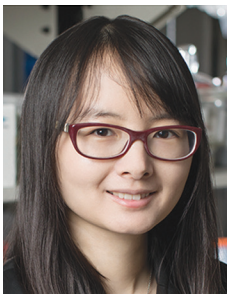

Qian Chen has been an assistant professor in the Department of Materials Science and Engineering at the University of Illinois at Urbana-Champaign since 2015. She received her PhD degree from the same department in 2012. Her research focuses on electron microscopy-based imaging, understanding, and engineering of soft materials, such as nanoparticle and colloidal self-assembly, protein transformation, battery materials, and energy-efficient filtration. Her awards include the American Chemistry Society (ACS) Victor K. LaMer Award in 2015, the Air Force Office of Scientific Research Young Investigator Program (AFOSR YIP) Award in 2017, the National Science Foundation CAREER Award in 2018, an Alfred P. Sloan Research Fellowship in 2018, and the ACS Unilever Award (2018). She also was recognized on the Forbes 30 Under 30 Science List in 2016. Chen can be reached by email at qchen20@illinois.edu.

Jong Min Yuk has been an associate professor in the Department of Materials Science and Engineering at the Korea Advanced Institute of Science and Technology (KAIST), Korea, since 2016. He received his PhD degree from KAIST in 2012. His research includes the development of the graphene liquid cell, and his current research focuses on *in situ* graphene liquid cell electron microscopy of liquid samples, such as bio-, energy-, and nanomaterials. Yuk can be reached by email at jongmin.yuk@kaist.ac.kr.

Matthew Hauwiller is a postdoctoral researcher in the Department of Materials Science and Engineering at the Massachusetts Institute of Technology. He received his PhD degree from the University of California, Berkeley, in 2019. His research focuses on understanding the nanoscale dynamics and structure of metallic and semiconductor materials using electron microscopy. Hauwiller can be reached by email at mhauwill@mit.edu.

Jungjae Park is a doctoral candidate in the Department of Materials Science and Engineering at the Korea Advanced Institute of Science and Technology (KAIST), Korea. He received his BS and MS degrees in mechanical science and engineering from Pusan National University, Korea, on and KAIST, respectively. His research focuses on the development of next-generation graphene liquid cell platforms, and direct observation of soft materials and their dynamic behavior using graphene liquid cells, including self-assembly of protein or biopolymers, and the interaction between extracellular vesicles. Park can be reached by email at jungjae10@kaist.ac.kr.

Kyun Seong Dae is a doctoral candidate in the Department of Materials Science and Engineering at the Korea Advanced Institute of Science and Technology, Korea. He received his BS degree in materials science and engineering from Hanyang University, Korea. His research focuses on mineralization and flocculation mechanisms by utilizing *in situ* liquid transmission electron microscopy. Dae can be reached by email at ddalgi1051@kaist.ac.kr.

Jae Sung Kim is a master's candidate in the Department of Materials Science and Engineering at the Korea Advanced Institute of Science and Technology, Korea. He received his BS degree in materials science and engineering from the University of Seoul, Korea. His research focuses on direct observation biomineralization using liquid cells and the demonstration of nucleation and phase transition pathways in the mineralization process. Kim can be reached by email at ijs7596@kaist.ac.kr.

Paul Alivisatos is the executive vice chancellor and provost and Samsung Distinguished Professor of Nanoscience and Nanotechnology at the University of California (UC), Berkeley. He is also the founding director of the Kavli Energy Nanoscience Institute, and Director Emeritus of Lawrence Berkeley National Laboratory. He is a founder of Nanosys and Quantum Dot Corp., now a part of Life Tech. His research includes the studies of the scaling laws governing the optical, electrical, structural, and thermodynamic properties of nanocrystals. He assisted in the establishment of the Molecular Foundry, a US Department of Energy Nanoscale Science Research Center, and was the facility's founding director. He is the founding editor of *Nano Letters*. Alivisatos can be reached by email at paul.alivisatos@berkeley.edu.